American Mineralogist, Volume 93, pages 1338–1348, 2008

Crystal chemistry of the mixed-layer sequence talc–talc-smectite–smectite from submarine hydrothermal vents

JAVIER CUADROS,[1,*] VESSELIN M. DEKOV,[2] AND SAVERIO FIORE[3]

[1]Department of Mineralogy, Natural History Museum, Cromwell Road, London SW7 5BD, U.K.
[2]Department of Geology and Palaeontology, University of Sofia, 15 Tzar Osvoboditel Blvd., 1000 Sofia, Bulgaria
[3]Istituto di Metodologie per l'Analisi Ambientale, CNR, Tito Scalo (PZ), Italy

ABSTRACT

Clay samples of hydrothermal origin from several oceanic spreading centers were studied using XRD, microprobe, infrared, and thermal analysis. They are talc, smectite, and mixed-layer talc-smectite (T-S) where the talc layers have several degrees of crystalline order. The smectite is trioctahedral in most cases, but there is also dioctahedral smectite both as mixed-layer and as a separate phase. All specimens contain Fe^{3+}, some of them in moderate amounts (up to 17% Fe_2O_3) distributed between the tetrahedral and octahedral sheets (maximum values: $^{IV}Fe = 0.32$, $^{VI}Fe = 0.68$, per $O_{10}[OH]_2$). Octahedral Fe abundance correlates with the presence of molecular water that is lost in a well-defined dehydration event above 200 °C. This water does not cause layer expansion and is interpreted to be present within the pseudo-hexagonal cavity, next to Fe^{3+} ions that generate a local charge imbalance. The presence of octahedral Fe^{3+} is accompanied by vacancies in the octahedral sheet to balance the excess positive charge. An infrared band at ~790 cm^{-1} is assigned to OH bending in the group Fe-Mg-□-OH. Analysis of this band suggests a range of short-range Fe-□ distributions, from random to ordered. Our sequence talc, T-S, trioctahedral smectite is defined by an increasing Al for Si substitution in the tetrahedra and increasing crystal disorder. The presence of Fe also causes crystal defects. This mixed-layer series can be considered as a continuum generated by the combination of chemical and crystal defect variability. Kerolite was used to designate disordered, hydrated talc. We find that there is no clear line delimiting talc from kerolite as a single phase or in mixed-layer minerals and that it is better to use a descriptive term for the latter such as "disordered talc." Dioctahedral smectite is also a possible end-member of the mixed-layer sequence, which implies an Al + □ for Mg substitution in the octahedral sheet. If T-S consists of polar TOT layers, the existence of dioctahedral smectite in T-S raises the question of the actual composition of the octahedral sheets within polar TOT layers.

Keywords: Crystal chemistry, infrared spectroscopy, kerolite, talc, talc-smectite, thermal analysis, trioctahedral smectite, X-ray diffraction

INTRODUCTION

Kerolite is a mineral name now discredited by the IMA Commission on New Minerals, Nomenclature and Classification, although recent literature uses this term. It designated disordered, hydrated talc (Brindley et al. 1977). In this paper, the term is used when referring to previous work where it was used. Two or more of the mineral phases—talc, kerolite, mixed-layer kerolite-smectite (Ker-S), and trioctahedral smectite—have been found in sediments of alkaline paleolakes (Eberl et al. 1982; Martin de Vidales et al. 1990; Pozo and Casas 1999), hydrothermally altered basaltic rocks (Elton et al. 1997), and hydrothermally altered ocean sediments (Koski et al. 1985, 1994). Given their similar composition and crystal structure, there has been confusion among these phases in some cases, especially when they were minor components in the sediment. There has been also a controversy about the nature of some specimens, whether they are smectite or Ker-S, according to the old term. Elton et al. (1997) provided an excellent summary of this controversy and of studies reporting one or several of these minerals from natural and experimental systems. From many of these studies it is obvious that there exists a genetic link between the aforementioned mineral phases, and that relatively small changes in the ambient physico-chemical conditions determine which of them forms or predominates. Here, we report on the crystal chemistry of talc, talc-smectite (T-S), and smectite of hydrothermal origin from ocean spreading centers and conclude with Eberl et al. (1982) that they should be regarded as a continuous sequence. We have found that dioctahedral smectite can also be interstratified with talc layers and thus be a third end-member of this mixed-layer series.

MATERIALS AND METHODS

We studied 19 samples of phyllosilicates from samples of sediment, anhydrite chimneys, and massive sulfide fragments collected from several submarine hydrothermal vent fields. The locations and description of the samples are given elsewhere (Dekov et al. 2008). We selected visually the subsamples with a phyl-

* E-mail: j.cuadros@nhm.ac.uk

losilicate appearance. They were air-dried and finely ground in an agate mortar. Their mineralogy was studied on random powder mounts by X-ray diffraction (XRD), using a position-sensitive detector (Enraf-Nonius Powder Diffraction System 120), with monochromatic Cu*K*α radiation, at 40 kV, 35 mA, with a 0.24 × 5 mm divergence slit and no receiving slit, in the range 2–120 °2θ. This type of apparatus collects the diffracted radiation in the entire angular range simultaneously, using an arch-shaped detector. The angle between the incident beam and the sample plane was 2–3°. The samples were spun to maximize the analyzed volume and the counting time was 15 min. We used Si, Y_2O_3, and $C_{22}H_{44}O_2{\cdot}Ag$ as calibrants. The samples with >2 wt% of non-phyllosilicate components [silicate phases (quartz, feldspars, etc.), FeOOH, and calcite] were purified through centrifugation (separation of the <2 μm size fraction), the dithionite-citrate-bicarbonate method of Mehra and Jackson (1960; to eliminate FeOOH), and acid dissolution at pH = 4 using HCl (to eliminate calcite). Oriented mounts were prepared by dispersing the specimens in water, placing a few drops of the dispersion in a glass slide and letting them dry (10 mg/4 cm^2). The samples were analyzed as air-dried and ethylene glycol-solvated (24 h in a glycol-saturated atmosphere at 60 °C) by XRD (Philips PW 1050) with monochromatic Cu*K*α radiation, graphite secondary monochromator, 1° divergence slit, 0.1 mm receiving slit, at 42 kV and 42 mA, scanning from 2 to 40 °2θ, with steps of 0.05 °2θ, at 8 s/step. Randomly oriented specimens were produced by side-loading to study the 060 diffraction peaks. In this case, the analysis conditions were 57–64 °2θ, 0.02 °2θ scanning steps, and counting time of 120 s/step.

Some of the clay phases were mixed-layers of non-swelling (talc) and swelling layers (smectite). We estimated the percentage of smectitic layers in these phases by modeling the XRD patterns of the oriented mounts, using the program MLM by Plançon and Drits (2000). This program calculates XRD patterns of 00*l* diffraction series of mixed-layer clay minerals with several intercalates. The variables used in the calculations are the relative proportions of the two layer types, layer *d*-spacing, type of layer-stacking order (R), size of the coherent scattering domain in the **c*** direction, and the chemical composition. Some of the samples contained more than one clay mineral phase. We estimated their relative abundance by adding the calculated patterns in the appropriate proportion to match the experimental patterns. One of the specimens (1183-9) was modeled using the program NEWMOD (Reynolds and Reynolds 1996), similar to MLM.

The major-element composition was determined at the Natural History Museum, London, using an electron microprobe (Cameca SX50) at 15 keV and 13 nA, with an electron beam diameter of 1 μm. The samples were prepared as polished sections with a flat surface and ~10 mineral grains were analyzed per sample. Certified natural oxides and salts were used as standards. The chemical analyses of the individual grains that were compatible with 2:1 phyllosilicates were selected (3–10 analyses, typically 5–6) and their compositions averaged. The chemical compositions were converted into structural formulas assuming a negative charge of 22 [$O_{10}(OH)_2$]. Some of the analyses indicated contamination with a silica phase. In these cases, silica was subtracted to obtain 4 Si atoms per $O_{10}(OH)_2$. Iron was found to be Fe^{3+} by the match between the lattice negative charge and the positive charge of the interlayer cations. The number of tetrahedral cations was fixed to 4 by placing in the tetrahedral sites the available Si, then Al, and then Fe as required. The maximum octahedral occupancy was fixed at 3. Fourier-transform infrared (FTIR; Perkin Elmer Spectrum One) analysis was performed at the Natural History Museum, London, in transmission mode on samples prepared as KBr pellets (sample/KBr ratio of 1/200 mg). Spectra were recorded from 4000 to 250 cm^{-1}, at 8 cm^{-1} resolution, with 8 scans acquired for each spectrum. The intensity of some of the IR bands was quantified by performing curve-fitting of the corresponding part of the spectrum, using the computer program Galactic Grams/AI (version 7.01). The bands were modeled as Gaussian-shaped. Thermogravimetry (TG; Seiko Exstar 6000) analysis was performed at the Instituto di Metodologie per l'Analisi Ambientale, Tito Scalo, Italy, on 9–12 mg samples, in platinum crucibles, from 20 to 1035 °C, with a 10°/min heating rate, reference of Al_2O_3, and a N_2 flow. The derivative of the TG diagram (DTG) was also obtained.

Results

XRD

Some representative XRD patterns of the oriented mounts are shown in Figure 1. They range (top to bottom) from talc to talc-rich T-S, smectite-rich T-S, and smectite. The mixed-layer samples were initially recognized by their irrational 00*l* series, but we noticed that mixed-layering in specimens with very few expandable layers was also indicated by other features. Glycolation produced (1) a narrowing of the 001 peak and a slight displacement toward lower *d*-spacing values, and (2) a decrease of the 003 peak intensity. The relative intensity of some of the peaks in the calculated patterns did not reproduce well due to an incorrect response of the program MLM to Fe content in the specimens. Also, the intensity of the calculated patterns below 5 °2θ is usually above that of the experimental ones because the effective size of the coherent scattering domain depends on the diffraction angle, and the program cannot simulate this effect (Plançon 2002). However, the peak positions and width that determine the composition of the mixed-layer mineral are correct. In a few cases (e.g., Fig. 1h), the pattern of the air-dried specimen was too complex, owing to inhomogeneous hydration of the smectite layers, and it was not simulated.

Table 1 shows the results of the XRD analysis. Many specimens have more than one T-S phase. The type of layer stacking in mixed-layer phases is always random (*R*0). The width of the 00*l* peaks indicates that the size of the coherent scattering domain in the **c*** direction generally decreases from talc to talc-rich T-S to smectite-rich T-S. This value was assessed in the calculated samples using the range of layers in the coherent scattering

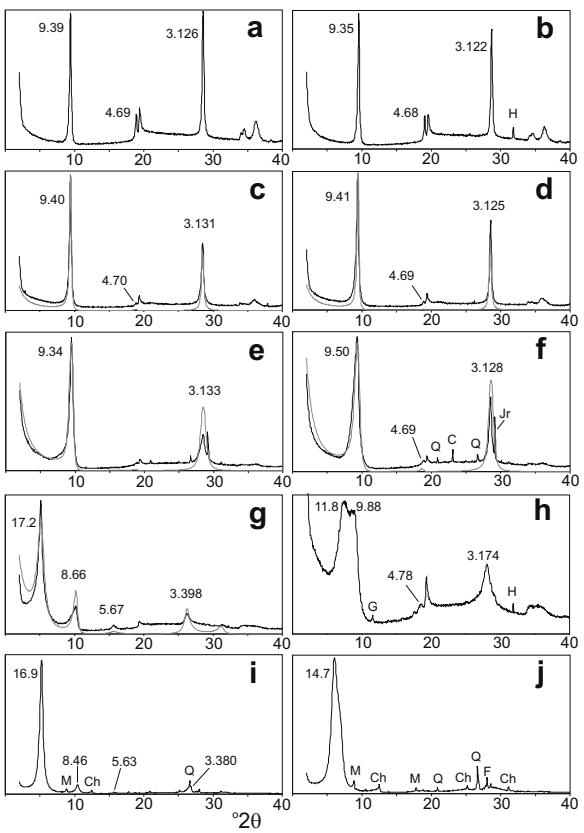

Figure 1. XRD patterns of oriented glycolated (left) and air-dry (right) mounts. The gray lines correspond to calculated patterns. The *d*-spacing values are in Å. (**a**, **b**) L1-86-NC-15D-2A, talc; (**c**, **d**) 1183-9, T-S with 2% smectite layers (% S); (**e**, **f**) 7D-8b1, T-S with 5% S; (**g**, **h**) 2251-2-3, T-S with 70% S; (**i**, **j**) L1-86-NC-27G-77-80, smectite. C = calcite, Ch = chlorite, F = feldspar, H = halite, Jr = jarosite, M = mica, Q = quartz.

domain (N) and the mean number of layers (N_{mean}, Table 1). Some of the samples were modeled with N = 1–300, which is an unrealistic value and only indicates a very large coherent scattering domain. Sample 1183-9, with sharp 00*l* peaks, was modeled with NEWMOD and yielded N = 1–40, a more realistic value. Accordingly, the maximum number of N in samples with large coherent scattering domains is probably in the range 40–60. The relative intensity of the 00*l* peaks allowed assessing the presence of Fe in the clay structure, as increasing Fe produces a relative increase of the 001 peak over the 002 and 003 peaks. The most Fe-rich specimen is 1183-9 (Table 1; Figs. 1c and 1d). Some samples contain chlorite and chlorite-smectite, which were quantified in one case (L1-86-NC-15D-3A) by including these two phases in the modeling process.

Many of the mixed-layer phases would have been described previously as Ker-S. Indeed, we find that there is no clear-cut limit between T-S and Ker-S. There were two main features by which talc and kerolite were distinguished. The first is their *d*-spacing value: ~9.38 Å for talc and ~9.6 Å for kerolite. The second feature is the number of defects in their layer stacking: low for talc and high for kerolite (Brindley et al. 1977). However, as the different *d*-spacing is produced by layer hydration, and hydration can be partial, there can be intermediate *d*-spacing values. The same is true of imperfect layer stacking. The problem becomes more acute when the layers are interstratified with other layer types. In our samples, we observed a rather narrow range of *d*-spacing values (9.35–9.40 Å) for the non-expandable component, which would correspond to talc (Table 1). However, the shape of the XRD patterns indicates different degrees of stacking order even for samples with the same proportion of expandable layers and *d*-spacing value of the non-expandable component. An example is sample 1183-9 (Figs. 1c and 1d), with 2% of smectite layers. By comparing this specimen with the talc patterns in Figures 1a and 1b, it can be seen that the sharpness of the 00*l* peak series indicates a similar thickness of the coherent scattering domains along **c***, but the *hkl* peaks of the talc specimen are better resolved than those of sample 1183-9, indicating rotational layer stacking defects in the latter. These differences cannot be assigned to the small 2% of smectite layers, and some of these rotational defects must occur between non-expandable layers. Thus, there is a range of crystalline order for T-S specimens within a narrow smectite layer content.

TABLE 1. Mineralogy of the investigated samples

Sample	Clay minerals (%)	%S layers	R*	Tot. %S†	*d*-spacing talc, ker (Å)	*N* (N_{mean})‡	Type of smectite§	Comment	Traces of other minerals‖
L1-86-NC-15D-2A	talc (100)				9.39				
L1-86-NC-15D-2-2	talc (100)				9.35				
L1-86-NC-15D-2-1	talc (100)				9.35				
	smectite (traces)								
	chlorite (traces)								
L1-86-NC-15D-2-3B	talc (100)				9.39			Fe in talc	G, Q
	chlorite (traces)								
L1-86-NC-15D-2-4	talc (100)				9.35			Fe in talc	G
	smectite (traces)								
	chlorite (traces)								
1183-9	talc-smectite (100)	2	0		9.39#	1–40 (25)	tri-	Fe-rich	
2251-2-3	talc-smectite 1 (66)	80	0	70	9.38#	1–20 (8)	tri-	little Fe in talc	G
	talc-smectite 2 (34)	50	0		9.38#	1–12 (5)	tri-	little Fe in talc	
2251-1-1a	talc-smectite 1 (62)	80	0	69	9.38#	1–20 (8)	tri-		G, Crist?,
	talc-smectite 2 (38)	50	0		9.38#	1–12 (5)	tri-		Mrb?
7D-8b1	talc-smectite (100)	5	0		9.38#	1–300 (10)	tri-	Fe in talc	Jr, Q, C
7D-27A1 GCS	talc-smectite (98)	5	0	7	9.38#	1–20 (10)	tri-	Fe in talc	Jr, F
	smectite (2)						tri-		
SL 347 GC 60-80	talc-smectite (100)	5	0		9.40#	1–300 (13)	tri-		Py
SL 347 GC 140-160	talc-smectite (100)	5	0		9.40#	1–300 (13)	tri-		
SL 347 GC 160-180	talc-smectite (100)	5	0		9.40#	1–300 (13)	tri-		
SL 347 GC 200-220	talc-smectite 1 (95)	10	0	13	9.40#	1–300 (13)	tri-	Fe in talc (?)	
	talc-smectite 2 (5)	60	0		9.40#	1–10 (5)	tri-		
SL 347 GC CC	talc-smectite 1 (96)	10	0	12	9.40#	1–300 (13)	tri-	Fe in talc (?)	
	talc-smectite 2 (4)	50	0		9.40#	1–9 (4)	tri-		
S2227-15	talc-smectite 1 (86)	10	0	13	9.40#	1–20 (10)	tri-		C
	talc-smectite 2 (4)	70	0		9.40#	1–9 (5)	tri-		
	serpentine (10)					1–18 (9)		chrysotile (?)	
L1-86-NC-15D-2-8	talc (52)			40	9.39	1–300 (16)			Q, F
	talc-smectite (34)	80	0		9.38#	1–15 (5)	di-		
	smectite (13)					1–15 (5)	di-		
L1-86-NC-15D-3A	talc-smectite 1 (27)	5	0	38	9.38#	1–20 (15)	tri- (?)		Crist, F
	chlorite (25)					1–15 (6)			
	chlorite-smectite (17)	48	1			1–15 (7)	di-		
	talc-smectite 2 (17)	40	0		9.38#	1–20 (15)	di- (?)		
	smectite (14)					1–14 (5)	di-	Fe-rich smectite	
L1-86-NC-27G-77-80	smectite (100)						tri(di)-		M, Q, G
	chlorite (traces)								

* Layer stacking order.
† Total % smectite layers from talc, T-S, and smectite (serpentine, chlorite, and chlorite-smectite not included).
‡ Range (and mean) number of layers in the X-ray coherent scattering domains.
§ Di- or tri-octahedral.
‖ C = calcite, Crist = cristobalite, F = feldspar, G = gypsum, Jr = jarosite, M = mica, Mrb = mirabilite, Py = pyrite, Q = quartz.
Values from the pattern simulations.

Figure 2 shows some of the patterns of the slow XRD scans with the 060 and adjacent peaks. The position of the 060 peaks indicates that the smectite interstratified with talc is trioctahedral, with the exception of L1-86-NC-15D-2-8, where it appears to be dioctahedral. In sample L1-86-NC-27G-77-80 (smectite with no mixed-layering), there is a large trioctahedral component (1.535 Å, Fig. 2e) and a smaller peak (1.510 Å) that we interpret as a minor dioctahedral component. The width and degree of resolution of the 060 and adjacent *hkl* peaks indicates the degree of crystal perfection, which decreases generally from talc to T-S as the proportion of smectite layers in T-S increases. Figure 2a shows the three diffraction peaks of a well-crystallized talc. As crystal order diminishes, the peak at 1.56 Å (242) decreases in intensity and that at 1.51 Å (330) becomes unresolved. The XRD analysis of the powder samples in the 0–120 °2θ range allowed the identification of the accessory mineral phases indicated in Table 1.

Chemical analysis

The chemical data (Tables 2 and 3) indicate a group of trioctahedral 2:1 phyllosilicates. In some samples, several grains yielded an SiO_2 excess that we interpreted as produced by contamination with a silica phase. It is impossible to assess how much silica corresponds to such a phase, so we subtracted silica to an assumed value of 4 Si atoms per $O_{10}(OH)_2$. This assumption is acceptable as the corrected analyses correspond to talc and T-S with a low smectite content. SEM observation of similar samples from other locations (on-going study) showed disordered talc and talc-rich T-S with a collomorph morphology resembling amorphous silica. It is possible that amorphous silica precipitates near or within the hydrothermal vents were the precursors of talc and talc-rich T-S in some of our samples, thus explaining the silica traces in some grains. Iron is present as Fe^{3+}, as evidenced by the good match between the lattice and interlayer cation charge in the resulting structural formulas. Had Fe^{2+} been present, there would be an excess lattice charge not balanced by the interlayer cations. Iron abundance is high in some samples. In those cases, the IR (see below) and the XRD analyses (relative intensity of 00*l* peaks, position of the 060 peak) indicate that the silicate 2:1 structure is Fe-rich, and they do not detect any other Fe phase. Iron was distributed between the tetrahedral and the octahedral sheets. According to what is found in other 2:1 phyllosilicates, we assumed that vacancies are more likely to occur in the octahedral than in the tetrahedral sheet. The amount of Al is generally low and increases with increasing smectite layers.

IR data

The IR spectra (Fig. 3) correspond to trioctahedral 2:1 phases, with an intense OH-bending band at ~670 cm^{-1} that envelopes several M_3OH bands (M = metal), sharp OH-stretching bands at 3680–3645 cm^{-1} corresponding to M_3OH groups, and the typical trioctahedral-type band system with a single main maximum at ~460 cm^{-1} (Russell and Fraser 1994). The spectra also indicate the absence of any amorphous Fe phase that might have escaped detection in the XRD analysis and confirmed the existence of Fe-rich samples. This feature is indicated by several OH-stretching bands, corresponding to Mg_3-OH (3677 cm^{-1}), Mg_2Fe-OH (3660 cm^{-1}), and $MgFe_2$-OH (3644 cm^{-1}). Given the high Fe content in some of the samples, we considered the possibility that minnesotaite (talc-like Fe end-member) was present. Minnesotaite has a structure and chemical formula differing from those of a trioctahedral 2:1 phyllosilicate (Guggenheim and Eggleton 1988). The sharp minnesotaite OH-stretching band at ~3500 cm^{-1} (Gadsden 1975) does not appear in any of the spectra of our Fe-rich specimens. Because the IR data are most sensitive for detecting the presence of a minor mineral phase,

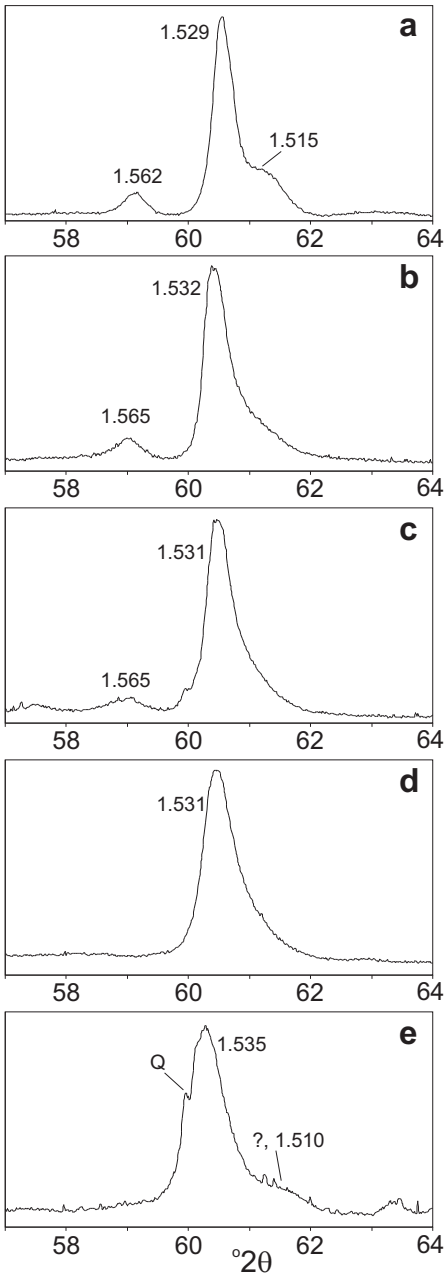

FIGURE 2. XRD patterns of the 060 peak region. The *d*-spacing values are in Å. (**a**) L1-86-NC-15D-2A, talc; (**b**) 1183-9, T-S with 2% smectite layers (% S); (**c**) 7D-8b1, T-S with 5% S; (**d**) 2251-2-3, T-S with 70% S; (**e**) L1-86-NC-27G-77-80, smectite. Q = quartz.

TABLE 2. Average major-element composition (in wt%) of the studied samples

Sample	Mineral	SiO_2	Al_2O_3	MgO	Fe_2O_3*	MnO	TiO_2	Cr_2O_3	ZnO	CuO	CaO	Na_2O	K_2O
L1-86-NC-15D-2A	talc	66.68†	0.26	32.04	0.73	0.03	0.01	0.03	0.08	0.03	0.02	0.11	0.04
L1-86-NC-15D-2-2	talc	66.31†	0.51	31.49	1.49	0.01	0.01	0.01	0.04	0.02	0.02	0.19	0.05
L1-86-NC-15D-2-1	talc	66.25†	0.39	32.12	0.95	0.01	0.03	0.03	0.10	0.03	0.01	0.12	0.04
L1-86-NC-15D-2-3B	talc	66.21	0.28	29.85	3.71	0.04	0.05	0.00	0.06	0.00	0.03	0.10	0.04
L1-86-NC-15D-2-4	talc	67.05†	0.29	30.54	1.96	0.01	0.00	0.00	0.11	0.01	0.03	0.14	0.04
1183-9	talc-smectite	61.50	0.69	21.64	16.77	0.12	0.01	0.02	0.17	0.37	0.02	0.34	0.01
2251-2-3	talc-smectite	60.88	3.24	28.20	7.73	0.18	0.00	0.02	0.07	0.62	0.10	0.48	0.14
2251-1-1a	talc-smectite	58.57	3.64	28.76	6.45	0.16	0.15	0.02	0.04	1.70	0.16	0.81	0.17
7D-8b1	talc-smectite	62.53	0.95	25.21	11.04	0.42	0.03	0.01	0.24	0.13	0.05	0.45	0.02
7D-27A1 GCS	talc-smectite	57.40	0.98	26.36	16.01	0.13	0.01	0.00	0.22	0.08	0.04	0.30	0.06
SL 347 GC 60-80	talc-smectite	65.26	1.74	32.30	0.41	0.02	0.01	0.03	0.01	0.01	0.09	0.16	0.01
SL 347 GC 140-160	talc-smectite	66.41	0.54	32.43	0.39	0.03	0.03	0.02	0.00	0.00	0.06	0.11	0.02
SL 347 GC 160-180	talc-smectite	66.75†	0.61	32.23	0.14	0.03	0.01	0.02	0.01	0.01	0.05	0.13	0.04
SL 347 GC 200-220	talc-smectite	66.58†	0.60	32.42	0.19	0.00	0.01	0.03	0.01	0.00	0.05	0.10	0.03
SL 347 GC CC	talc-smectite	66.32	1.54	31.48	0.32	0.04	0.01	0.01	0.01	0.00	0.09	0.17	0.04
S2227-15	talc-smectite	66.00	0.64	32.81	0.02	0.03	0.01	0.01	0.01	0.04	0.13	0.24	0.06
L1-86-NC-15D-2-8	talc, talc-smectite	56.09	13.93	25.16	3.33	0.03	0.05	0.04	0.06	0.07	0.08	1.06	0.43
L1-86-NC-15D-2-3A	talc-smectite	57.38	7.90	32.91	1.39	0.02	0.09	0.03	0.07	0.02	0.02	0.26	0.05
L1-86-NC-27G-77-80	smectite	51.36	11.98	23.79	10.87	0.09	0.41	0.03	0.10	0.02	0.22	1.88	0.34

* Total Fe expressed as Fe_2O_3.
† Apparent excess silica was subtracted.

TABLE 3. Average structural formulas of the studied samples

Sample	Si	^{IV}Al	$^{IV}Fe^{3+}$	^{VI}Al	^{VI}Mg	$^{VI}Fe^{3+}$	Mn	^{VI}Ti	^{VI}Zn	^{VI}Cu	Mg int	Ca	Na	K	Σ int	Σ oct	Int. charge
L1-86-NC-15D-2A	4.00*	0.00	0.00	0.02	2.91	0.03	0.00	0.00	0.00	0.00	0.00	0.00	0.01	0.00	0.02	2.97	0.02
L1-86-NC-15D-2-2	3.99*	0.01	0.00	0.03	2.85	0.07	0.00	0.00	0.00	0.00	0.00	0.00	0.02	0.00	0.03	2.95	0.03
L1-86-NC-15D-2-1	3.99*	0.01	0.00	0.02	2.89	0.04	0.00	0.00	0.00	0.00	0.00	0.00	0.01	0.00	0.02	2.96	0.02
L1-86-NC-15D-2-3B	4.00	0.00	0.00	0.02	2.71	0.17	0.00	0.00	0.00	0.00	0.00	0.00	0.01	0.00	0.02	2.90	0.02
L1-86-NC-15D-2-4	4.00*	0.00	0.00	0.02	2.81	0.09	0.00	0.00	0.00	0.00	0.00	0.00	0.02	0.00	0.02	2.93	0.02
1183-9	3.84	0.05	0.11	0.00	2.01	0.68	0.01	0.00	0.01	0.02	0.00	0.00	0.04	0.00	0.04	2.72	0.04
2251-2-3	3.75	0.23	0.02	0.01	2.59	0.29	0.01	0.00	0.00	0.03	0.00	0.01	0.06	0.01	0.08	2.93	0.08
2251-1-1a	3.65	0.27	0.08	0.00	2.67	0.22	0.01	0.01	0.00	0.08	0.00	0.01	0.10	0.01	0.12	2.99	0.13
7D-8b1	3.86	0.07	0.07	0.00	2.32	0.45	0.02	0.00	0.01	0.01	0.00	0.00	0.05	0.00	0.06	2.81	0.06
7D-27A1GCS	3.61	0.07	0.32	0.00	2.47	0.45	0.01	0.00	0.01	0.00	0.00	0.00	0.04	0.00	0.04	2.95	0.05
SL 347 GC 60-80	3.90	0.09	0.01	0.03	2.86	0.07	0.00	0.00	0.00	0.00	0.01	0.01	0.02	0.00	0.04	2.97	0.05
SL 347 GC 140-160	3.99	0.01	0.00	0.03	2.91	0.03	0.00	0.00	0.00	0.00	0.00	0.00	0.01	0.00	0.02	2.96	0.02
SL 347 GC 160-180	4.00*	0.00	0.00	0.04	2.88	0.03	0.00	0.00	0.00	0.00	0.00	0.00	0.01	0.00	0.02	2.95	0.02
SL 347 GC 200-220	3.99*	0.01	0.00	0.03	2.90	0.03	0.00	0.00	0.00	0.00	0.00	0.00	0.01	0.00	0.02	2.96	0.02
SL 347 GC CC	3.95	0.05	0.00	0.06	2.80	0.08	0.00	0.00	0.00	0.00	0.00	0.01	0.02	0.00	0.03	2.94	0.03
S2227/15	3.96	0.03	0.01	0.01	2.93	0.03	0.00	0.00	0.00	0.00	0.00	0.01	0.03	0.00	0.04	2.98	0.05
L1-86-NC-15D-2-8	3.43	0.55	0.02	0.45	2.25	0.14	0.00	0.00	0.00	0.00	0.05	0.01	0.13	0.03	0.21	2.85	0.26
L1-86-NC-15D-2-3A	3.51	0.49	0.00	0.08	2.85	0.06	0.00	0.00	0.00	0.00	0.15	0.00	0.03	0.00	0.19	3.00	0.34
L1-86-NC-27G 77-80	3.25	0.75	0.00	0.15	2.23	0.51	0.01	0.02	0.01	0.00	0.00	0.02	0.15	0.03	0.20	2.92	0.21

* Apparent excess silica was subtracted.

we believe that minnesotaite is not present. The OH-stretching region of sample L1-86-NC-27G-77-80 shows a band at 3630 cm^{-1}, corresponding to an Al-rich dioctahedral phase, and the trioctahedral component as a shoulder at 3671 cm^{-1}. However, the rest of the spectrum is typical of a trioctahedral phase. This fact is explained because there is a minor amount of dioctahedral smectite in the sample and the absorptivity of the dioctahedral OH-stretching bands in smectite is much greater than that of trioctahedral OH-stretching bands (compare spectra in Russell and Fraser 1994). For all the samples, there is an evolution of the band system between 250 and 600 cm^{-1}, in which several bands become increasingly unresolved from talc to T-S to smectite. This trend indicates an increasing number of defects in the short-range atomic arrangement.

Thermal analysis

Some of the results of the thermal analysis are shown in Figure 4, with both the TG and DTG curves. Many of the diagrams are complex, with several thermal events, sometimes produced by several mineral phases. The thermal events are now described for the several temperature regions. In the 20–400 °C range, we observed the dehydration of the clay and other phases. Clay dehydration appeared as a single weight loss starting at 20 °C (e.g., Figs. 4a and 4e) or as a complex event with a main loss at ~200 °C (Figs. 4b and 4c). The differentiated dehydration event at ~200 °C is related to water strongly linked to the clay structure and we investigated whether it had been described in the literature. Faust et al. (1959) analyzed stevensite samples using differential thermal analysis (DTA) and found that dehydration started above 100 °C and had its peak at 150–160 °C. Mackenzie (1970) shows DTA diagrams of trioctahedral smectites with doubled-dehydration systems in which the second, smaller peak above 200 °C is related to the interlayer cation. These two cases refer to smectite minerals, whereas we found our high-temperature dehydration event in talc or talc-rich T-S, with very small interlayer charge and very few interlayer cations. Thus, the nature of this strongly linked water in our samples must be different from that in the afore mentioned references. However, Brindley et al. (1977) observed water-loss steps in kerolite samples above 200 °C similar to those in our Figure 4b and thus their results resemble ours. We examine this question in detail in the discussion section.

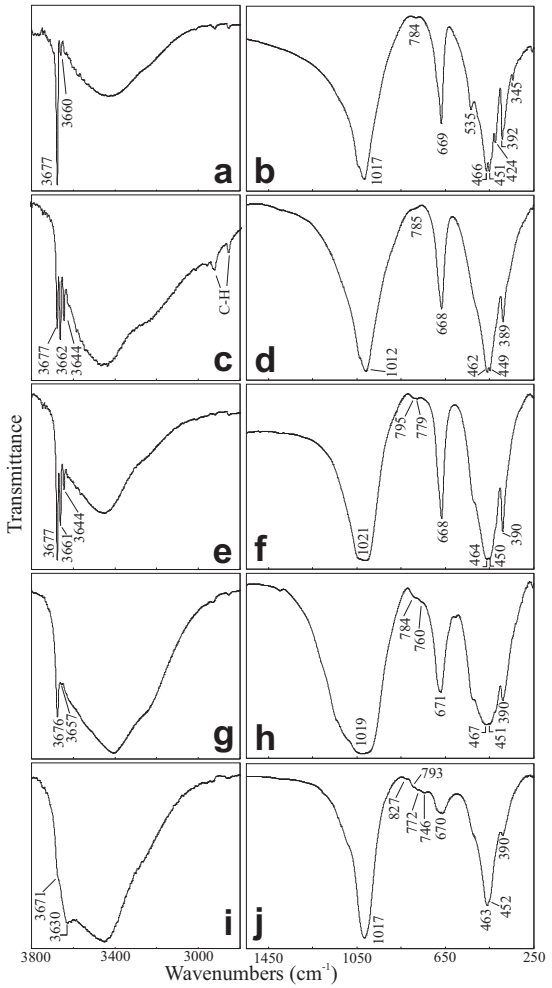

FIGURE 3. Relevant sections of the IR spectra of some representative samples. Band labels are in cm^{-1}. The wide band with a maximum at ~3500 cm^{-1} corresponds to OH stretching of the adsorbed water. (**a**, **b**) L1-86-NC-15D-2A, talc; (**c**, **d**) 1183-9, T-S with 2% S); (**e**, **f**) 7D-8b1, T-S with 5% S; (**g**, **h**) 2251-2-3, T-S with 70% S; (**i**, **j**) L1-86-NC-27G-77-80, smectite. C-H = stretching of the C-H bond in organic matter.

Dehydration is not completed at the low-temperature range, and it continues even at dehydroxylation temperatures (~800 °C). The amount of hydration water is roughly related to the proportion of smectite in the mixed-layer phases, as expected, and to the degree of crystal disorder (as indicated, for example, by the *hkl* reflections in XRD patterns), except when the high-temperature dehydration event is present. The relation between hydration water content and crystal defects has been recognized frequently, for example by Brindley et al. (1977) when comparing talc and kerolite, and by Brindley and Hang (1973) when comparing 7 and 10 Å garnierites (Ni-rich talc and kerolite, respectively). They also found residual hydration water loss up to dehydroxylation temperatures. In the 20–400 °C range in our samples, there are also dehydration reactions of other mineral phases such as gypsum (Fig. 4d), and other events that we could not identify. An example of the latter is the weight loss at 200 °C in Figure 4d, which seems to be a combination of strongly

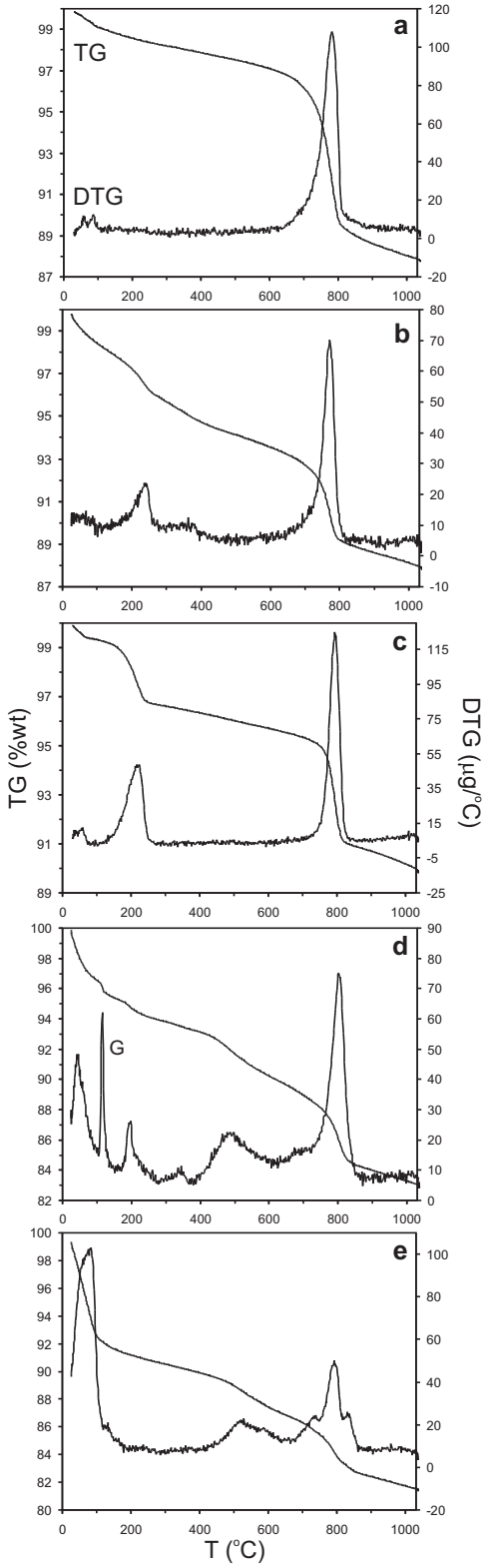

FIGURE 4. TG and DTG curves of some representative samples. (**a**) L1-86-NC-15D-2A, talc; (**b**) 1183-9, T-S with 2% S; (**c**) 7D-8b1, T-S with 5% S; (**d**) 2251-2-3, T-S with 70% S; (**e**) L1-86-NC-27G-77-80, smectite. G = gypsum.

linked water loss (wide peak in the DTG curve) and a sharp weight loss of unknown origin.

Between 400 and 700 °C, we found weight loss events that we could assign to thermal reactions in other mineral phases detected by XRD such as chlorite, dioctahedral smectite, jarosite, and serpentine (Table 1). The weight loss at ~500 °C in Figure 4e is compatible with dehydroxylation of a dioctahedral smectite, whose presence is indicated by XRD (Fig. 2e) and IR (Fig. 3i). We could not assign the large weight loss observed at ~500 °C in Figure 4d. The dehydroxylation of the trioctahedral 2:1 phyllosilicates began at 700 °C. The corresponding peaks in the DTG diagrams end at ~850 °C, although the TG lines show that the water loss continues up to the maximum temperature. Ideally, the weight loss of this reaction for a pure phase is ~5% but we found losses from 5 to 14%. Also, some of the samples showed multiple (usually two) events in this temperature range. This feature proved to be related to NaCl, present in many samples, which melts at ~800 °C. We found a very good correlation between Na content of the whole sample (obtained by ICP-AES) and the total weight loss above 700 °C. For further proof, a few samples with a weight loss 9–14% were washed repeatedly with distilled water and analyzed by TG, resulting in a weight loss of 5–6%. Besides, the dehydroxylation temperature of the washed samples moved to higher temperature (up to 100 °C higher). Thus, the thermal reaction of NaCl, probably involving loss of Cl_2 gas, causes dehydroxylation at a lower temperature. Figure 4e shows a multiple thermal event at 700–900 °C, in this case with three DTG maxima.

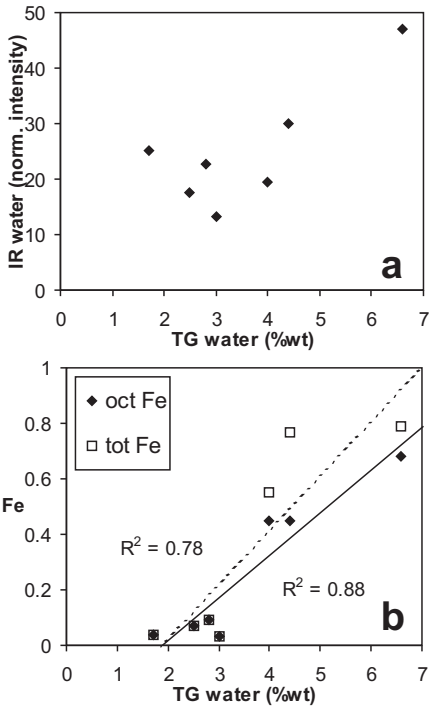

FIGURE 5. Plots of (**a**) the normalized intensity of the OH-stretching system of hydration water vs. the weight loss corresponding to hydration water, and (**b**) total and octahedral Fe content per $O_{10}(OH)_2$ vs. the same weight loss.

DISCUSSION

Water strongly linked to talc surface

The investigation of strongly linked water in talc-rich samples (loss at ~200 °C) is of interest as in a few cases, like that in Figure 4c, the proportion of this type of water is rather high. It is not evident how so much of water is retained at such high temperature as the layer charge and the amount of interlayer cations are small in these samples. We first tried to ascertain whether the weight loss corresponds to adsorbed molecular water. For this, we selected the samples that allow quantification of their adsorbed water by means of both IR and TG analysis. The conditions for the selection are that (1) the area of the IR spectra where OH stretching of adsorbed water appears (~3500 cm^{-1}) is free from other intense bands, and (2) the TG diagram shows only reactions of a trioctahedral 2:1 phase. We thus measured the intensity of the system of IR OH-stretching bands of both the adsorbed water and the structural OH groups, by curve-fitting, and normalized the intensities by calculating the ratio adsorbed water intensity/hydroxyl intensity. This normalization assumes that the hydroxyl-related intensity is the same for all samples, which is a good approximation. We also measured the weight loss between 20 °C and the onset of dehydroxylation in the TG diagrams. Figure 5a shows the plot of the IR- and TG-measured adsorbed water. There is a reasonable correlation except for one sample. Given that the TG and IR experiments were carried out in different locations, with different ambient relative humidity, we could only expect a rough correlation in this plot, and we conclude that the weight loss at ~200 °C corresponds to adsorbed water.

We then investigated what links this adsorbed water so strongly to the clay surface by plotting several chemical features vs. the amount of adsorbed water. We found a correlation with Fe content (Fig. 5b), good for total Fe and better for octahedral Fe. However, as tetrahedral Fe is rather low in most samples, we believe that the real physical relation corresponds to octahedral Fe. There was no correlation with tetrahedral Fe, of with layer, tetrahedral, or octahedral charge. It has been suggested that hydration water in kerolite released at 110–700 °C may be retained in the pseudo-hexagonal cavity of the tetrahedral sheet (Brindley et al. 1977). This is likely, as the small interlayer distance would favor the trapping of water in these cavities. However, our study shows that Fe helps to retain adsorbed water very efficiently. We interpret this fact in the following way: Fe^{3+} located in octahedra at the bottom of the pseudo-hexagonal cavity generates a local charge imbalance, which is counteracted by water molecules that penetrate the cavity and create a relatively strong hydrogen bond with the OH group. The water molecule has a diameter of ~2.8 Å, and the pseudo-hexagonal cavity one of 4.6–5.2 Å, which allows one water molecule per cavity. If this is correct, we should expect that octahedral Al produces the same effect but this is difficult to test in our samples as the amount of octahedral Al is generally very low. Adding octahedral Al values to octahedral Fe in Figure 5b produces a small increase [0.02–0.03 atoms per $O_{10}(OH)_2$] in the four lower datapoints and an insignificant increase in the R^2 value of the regression (0.88 to 0.89). In the absence of further proof, we can assume that a local excess of positive charge in the octahedral sheet produced by any cation with charge >2+ causes water molecules to be retained in the pseudo-hexagonal

cavity. Drits and McCarty (2007) have also described strongly linked water in illite that they interpret as being adsorbed within the pseudo-hexagonal cavities.

This finding is relevant for the hydration state of talc. It is assumed that talc with a *d*-spacing of 9.38 Å is not hydrated. However, if the hydration water is located in the pseudo-hexagonal cavity it may not cause interlayer expansion. This is the case in the three samples with high hydration water content in Figure 5b. Sample 1183-9 has a noticeable weight loss at 200–250 °C (Fig. 4b) and a large total content of adsorbed water (6.6 wt%), however, it has a *d*-spacing of 9.39 Å (Table 1) and the basal XRD peaks are sharp (Figs. 1c and 1d). Samples 7D-8b1 and 7D-27A1 GCS are talc-rich T-S. They have a large weight loss at ~200 °C (Fig. 4c; the diagram of 7D-27A1 GCS is very similar) but the *d*-spacing of their talc component is 9.38 Å. As indicated above, the strongly linked water cannot be in the smectite layers for two reasons: (1) dehydration would occur from the very start of the temperature increase, and (2) the very few smectite layers in these samples cannot account for the large dehydration step at 200 °C. Smectite layers are responsible only for the small water loss below 100 °C (Fig. 4c). Thus, our results show that layers with a *d*-spacing similar or equal to that defined for talc can be highly hydrated, with water probably located in the pseudo-hexagonal cavities.

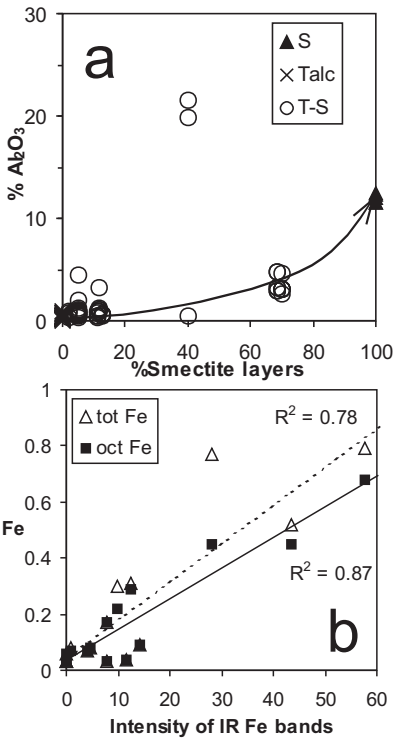

FIGURE 6. (**a**) Alumina content of the sequence talc, T-S, smectite vs. the percent smectite layers (datapoints are from individual grain analyses and not averaged values). The analyses correspond to the samples: L1-86-NC-15D series: -2A, -2-2, -2-1, -2-3B, and -2-4; 1183-9; 2251-2-3; 2251-1-1a; 7D-8b1; 7D27A1 GCS; complete SL series; S2227-15; L1-86-NC-15D-2-8; L1-86-NC-27G-77-80. (**b**) Iron content vs. the normalized intensity of IR Fe-related OH-stretching bands. Samples: L-1-86-NC-15D series: -2A, -2-2, -2-1, -2-3B, -2-4, -2-3A; 1183-9; 2251-2-3; 2251-1-1a; 7D-8b1; 7D-27A1 GCS; complete SL series. The arrow in **a** is only indicative of the trend.

Chemical composition

The sequence talc–T-S–smectite is likely to be characterized by an increase of cation substitution that causes an increase of the layer charge. This would cause the transition from the talc end-member, without layer charge, to smectite, with layer charge and hydrated interlayer cations. We found that this cation substitution is Al → Si in the tetrahedral sheet (Table 3). A plot at $\%Al_2O_3$ content vs. %S (Fig. 6a) shows a positive correlation. Only sample L1-86-NC-15D-2-8 is off the trend, with two of the analyses showing a very high Al_2O_3 content. This result is in agreement with our previous observation of the 060 XRD peak that indicates that smectite in this specimen is dioctahedral. The trend of increasing Al_2O_3 content becomes non-linear from ~70 %S but this may reflect the presence of a dioctahedral component in the smectite sample as indicated by IR, XRD, and TG (Figs. 3i, 2e, and 4e, respectively). Thus, Al for Si substitution in the tetrahedral sheet generates negative charge that is balanced by interlayer cations and produces smectite-type layers.

Some of the samples are Fe-rich, which is consistent with their seafloor vent site origin where Fe is one of the main dissolved species (Von Damm et al. 2005). This high Fe content in some of our samples was further investigated. As discussed above, we identified the necessary Fe in the tetrahedral sheet of the structural formula to obtain a complete tetrahedral occupancy. Previous authors have provided chemical analyses of kerolite-type materials with incomplete tetrahedral occupancy (Brindley et al. 1977; Léveillé et al. 2002) and octahedral occupancy >3 per $O_{10}(OH)_2$, although, in our opinion, most of these cases suggest contamination with a 1:1 Mg-rich phase as indicated by Brindley and Hang (1973). Like us, Brindley et al. (1979) identified Fe^{3+} in the tetrahedral sheet of their kerolite-pimelite series to complete the tetrahedral occupancy. We used our IR data to discriminate between tetrahedral and octahedral Fe, using the fact that the OH-stretching bands only reveal octahedral cations. We measured the intensities of the OH-stretching bands corresponding to metal groups, including Fe, by means of curve-fitting, and normalized them with respect to the total intensity of the OH-stretching system (total intensity = 100). We then plotted these values vs. the total and octahedral Fe content of the samples. If all Fe were located in the octahedral sheet, the correlation between the two sets of values would be better for total Fe content. Alternatively, if some of the Fe were located in the tetrahedral sheet, the correlation for our calculated octahedral Fe would be better. Figure 6b shows that our values of octahedral Fe correlate better with the IR data, and thus support our distribution of Fe in the octahedral and tetrahedral sheets.

We observed that the presence of significant Fe in the samples increased the concentration of crystal defects. For example, sample 1183-9 is a T-S with only 2 %S. The 00*l* peaks in this specimen are sharp and talc-like, but there is a clear decrease of crystalline perfection as compared with the talc samples with very low Fe content, as shown in the lower resolution and intensity of *hkl* peaks (Figs. 1c, 1d, and 2b) and in the lower resolution of the IR spectrum in the range of lattice vibrations (Fig. 3d, 600–200

cm^{-1}). Similarly, samples 7D-8b1 and 7D-27A1 GCS are T-S with 5 %S and high Fe content. Three other samples (SL series, Table 1) have the same layer composition but little Fe, and all of them display *hkl* XRD peaks and IR lattice vibrations that are better resolved. It can be inferred that the inclusion of Fe^{3+} in the lattice introduces crystal defects. As Fe^{3+} and Mg^{2+} have a very similar radius, the defects are probably related to the different charge. The presence of Fe^{3+} may force vacant sites in the octahedral sheet to maintain the charge neutrality, as it roughly occurs in our samples (Table 3), and both the vacant sites, and sites with a local excess of positive charge may cause the crystal defects. The presence of water in the pseudo-hexagonal cavities may be also a cause of disruption in the layer stacking.

Iron in these Fe-rich samples is contributed by the hydrothermal fluids (Von Damm et al. 2005; Butterfield et al. 1994; Lackschewitz et al. 2006). Although Fe is transported as Fe^{2+} by these fluids, it is oxidized by mixing with seawater. The mixing of hydrothermal fluids and seawater is evident by the presence of Mg, which is contributed by the latter.

Talc–T-S–smectite mixed-layer sequence

Our samples appear as a series of trioctahedral compositions from talc to smectite, where the increasing tetrahedral Al is the main factor in the increase of smectite layers. There is only one exception in the sequence, in which the smectite in T-S is dioctahedral (Table 1). This exception indicates that it is possible to have such mixed-layer system as talc and dioctahedral smectite. According to morphological and petrographic evidence, talc formed by precipitation from solution on the surface of the sediment and in the interior of open fissures near the sediment surface, whereas T-S with a range of compositions formed in the interior of sulfate chimney conduits, where Mg-rich seawater and Si-rich hydrothermal fluids mixed. We suggest that the proportion of smectite layers increases where there is less available Mg due to restricted access of seawater, as in the interior of chimney conduits, and that the available Mg/Al ratio controls the composition of the product. Our only fully smectitic specimen was cored from the sediment blanket at 77–80 cm below the seafloor. Following the same line of reasoning, we believe that it formed within the sediment, where Al is available from detrital minerals and where seawater access was restricted. The formation of T-S with dioctahedral smectite in sample L1-86-NC-15D-2-8 may have occurred under similar conditions. This sample was dredged from the sediment and contains dioctahedral smectite, smectite-rich T-S, and talc (Table 1). This assemblage suggests that talc formed on the surface of the sediment and that T-S and smectite formed within the sediment, where seawater penetration was small. Other factors such as precipitation kinetics and changes in porosity and water chemistry may have controlled partially the final mineral products within the sediment.

The mixed-layer series talc-T-S-smectite is the result of chemical differences that also cause structural variations. In our case, both Al and Fe enrichment are responsible for the increased crystal defects. However, the structural changes toward a less-orderly crystal structure in our samples are not the same at different crystal scales or in different crystal directions, with the result that the several experimental techniques show seemingly contrasting degrees of crystal perfection. Sample 1183-9 has sharp talc-like 00*l* XRD peaks, poorly developed *hkl* peaks (Figs. 1c and 1d), and a poorly resolved ("kerolite-like") IR spectrum (Figs. 3c and 3d). Sample 7D-8b1 has XRD patterns and IR spectrum that indicate a highly disordered structure (Figs. 1e, 1f, 3e, and 3f), although the TG-DTG diagram (Fig. 4c) has sharp thermal events that suggest a well-crystallized structure, as compared with those of the well-crystallized talc (e.g., Fig. 4a). We observed that the apparent sequence of crystalline order in our samples was commonly different depending on the technique used. These differences arise from the combination of differing chemical composition and crystallization environments. For example, Al and Fe enrichment affect the crystal structure differently, as discussed above. Thus, the relationship between composition and crystal perfection is complex. According to our results, there is no clear compositional or structural line between talc and "kerolite," and it is better to describe specimens as talc, disordered talc, T-S, and smectite. In agreement with Eberl et al. (1982), we believe that the adequate mode of representing this mixed-layer sequence is as a continuum of compositional and structural character, where the end-members are talc and trioctahedral smectite.

The introduction of dioctahedral smectite in the talc-smectite mixed-layer series would introduce dioctahedral smectite as a third end-member. This possibility raises interesting crystal-chemical questions in the mixed-layer phases given that one type of layer is dioctahedral and the other trioctahedral. It has been shown that layers in illite-smectite have a polar character, that is, it is the sequence TIT (T = tetrahedral sheet; I = interlayer) that defines the type of layer (illite or smectite), rather than the sequence TOT (O = octahedral sheet), and thus the T sheets on both sides of the TOT units are different (Altaner et al. 1988; Jakobsen et al. 1995). This fact explains why glycolation produces a complete contrast between smectite and illite layers (as layers expand completely or not at all) because the "layers" are in fact defined by the behavior of the interlayers. As T-S shows the same behavior upon glycolation, it is very likely that their layers are also polar. However, if the TOT units are half smectitic (dioctahedral) and half talc-like (trioctahedral), what is the actual composition of the O sheets in these polar TOT units? The structure of these phases would be a hybrid, with a sequence of talc- and smectite-like T sheets and interlayers, and dioctahedral and trioctahedral O sheets or domains.

Fe-Mg-□ sites

The amount of octahedral Fe^{3+} in our samples is roughly correlated with the number of octahedral vacancies, with ~0.5 vacancies per Fe atom, probably as a way of balancing the excess positive charge. It is likely that many of these vacancies are close to the Fe atoms as this would reduce local charge imbalance. Many of our IR spectra show a weak band at ~790 cm^{-1}, which could correspond to OH bending in MgFe-OH groups. To test this possibility, we measured the intensity of this band by means of curve-fitting, normalized their intensities with respect to the intense band at ~670 cm^{-1} (OH bending in a trioctahedral environment), and plotted them vs. the sum Fe + vacancies in the octahedral sheet (Fig. 7). We did not use samples in which a dioctahedral smectite component was found or suspected. The plot revealed three groups of samples following different pat-

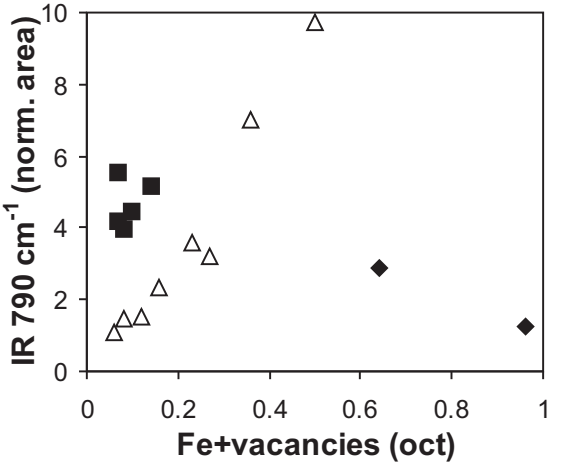

FIGURE 7. Plot of the normalized intensity of the IR band at 790 cm^{-1} vs. the sum of octahedral Fe and vacancies [per $O_{10}(OH)_2$]. The plot tests the hypothesis that this IR band corresponds to OH bending in the group FeMg-OH. The different symbols indicate different patterns (see text).

terns. One group (squares) corresponds to the SL sample series (Table 1), from the Grimsey Graben. They show no correlation. The second group (triangles) includes samples from different locations and shows a correlation between the two variables. The third group (diamonds) has two samples from different locations. The striking correlation of the triangles supports the assignment of the ~790 cm^{-1} band to MgFe-OH groups. The reason why the other two groups do not follow the same pattern is probably cation ordering in the octahedral sheet. Figure 8 shows that Fe-□ pairs may be next to two, one, or zero OH groups, contributing to IR OH-bending intensity in varying degrees or not at all. Possibly, the triangles in Figure 7 are the result of a random cation distribution, in which an increase of Fe + vacancies produces a proportional increase of the MgFe-OH band. The squares indicate an enhanced IR intensity with low Fe + vacancies values, which suggests ordering as in Figure 8b. For the squares, the Fe/Al ratio is ~1, which may contribute to the lack of correlation because the control on the number of Mg-M^{+3}-□ groups is exerted by both Al and Fe in different degree in the several specimens. The two diamonds suggest cation ordering with many Fe-□ pairs arranged as in Figure 8c. The vacancies also produce MgMg-OH pairs. FeFe-OH pairs are also likely to appear in Fe-rich samples and thus their corresponding IR bands should be observable. This seems to be the case because (1) a few samples display a maximum at ~800 cm^{-1}, assigned to FeFe-OH by Cuadros and Altaner (1998), and (2) there is a band in some other samples at ~760 cm^{-1}, which is a very likely position for the MgMg-OH band. As with the MgFe-OH groups, the intensities of MgMg-OH and FeFe-OH bands would be affected by cation ordering. Thus, if our interpretation is correct, these data show that the short-range octahedral cation arrangement can be very different in specimens of the talc-T-S mixed-layer series containing Fe and vacancies.

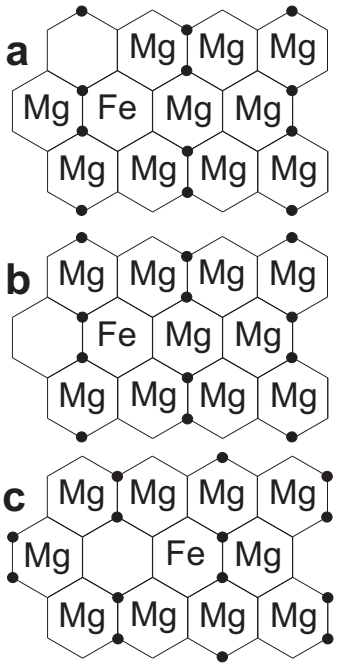

FIGURE 8. Representation of the octahedral sites of a trioctahedral mineral showing different arrangements of Fe-□ pairs and the hydroxyl groups (dots). The number of hydroxyls next to an Fe-□ pair is different for each arrangement: one (**a**), two (**b**), and zero (**c**).

ACKNOWLEDGMENTS

This study was supported by the Royal Society (grant 2005/R1-JP). We are very grateful to J.C. Alt (University of Michigan), D.E. Ames (Geological Survey of Canada), M. D'Orazio (University of Pisa), and T. Kuhn (IFM-GEOMAR, Germany) who provided the samples from the EPR, Juan de Fuca, St. Paul FZ, and Grimsey Graben, respectively, and to two anonymous reviewers for their valuable comments.

REFERENCES CITED

Altaner, S.P., Weiss, Jr., C.A., and Kirkpatrick, R.J. (1988) Evidence from ^{29}Si NMR for the structure of mixed-layer illite/smectite clay minerals. Nature, 331, 699–702.

Brindley, G.W. and Hang, P.T. (1973) The nature of garnierites—I. Structures, chemical compositions and color characteristics. Clays and Clay Minerals, 21, 27–40.

Brindley, G.W., Bish, D.L., and Wan, H.M. (1977) The nature of kerolite, its relation to talc and stevensite. Mineralogical Magazine, 41, 443–452.

Brindley, G.W., Bish, D.L., and Wan, H.M. (1979) Compositions, structures, and properties of nickel-containing minerals in the kerolite-pimelite series. American Mineralogist, 64, 615–625.

Butterfield, D.A., McDuff, R.E., Franklin, J., and Wheat, C.G. (1994) Geochemistry of hydrothermal vent fluids from Middle Valley, Juan de Fuca Ridge. In M.J. Mottl, E.E. Davis, A.T Fisher, and J.F. Slack, Eds., Proceedings of the Ocean Drilling Program, Scientific Results, 139, p. 395–410. U.S. Government Printing Office, Washington, D.C.

Cuadros, J. and Altaner, S.P. (1998) Compositional and structural features of the octahedral sheet in mixed-layer illite/smectite from bentonites. European Journal of Mineralogy, 10, 111–124.

Dekov, V.M., Cuadros, J., Shanks, W.C., and Koski, R.A. (2008) Deposition of talc–kerolite-smectite–smectite at seafloor hydrothermal vent fields: Evidence from mineralogical, geochemical and oxygen isotope studies. Chemical Geology, 247, 171–194, DOI: 10.1016/j.chemgeo.2007.10.022.

Drits, V. and McCarty, D. (2007) The nature of structure-bonded H_2O in illite and leucophyllite from dehydration and dehydroxylation experiments. Clays and Clay Minerals, 55, 45–58.

Eberl, D.D., Jones, B.F., and Khoury, H.N. (1982) Mixed-layer kerolite/stevensite from the Amargosa desert, Nevada. Clays and Clay Minerals, 30, 321–326.

Elton, N.J., Hooper, J.J., and Holyer, V.A. (1997) An occurrence of stevensite and kerolite in the Devonian Crousa gabbro at Dean Quarry, The Lizard, Cornwall, England. Clay Minerals, 32, 241–252.

Faust, G.T., Hathaway, J.C., and Millot, G. (1959) A restudy of stevensite and allied minerals. American Mineralogist, 44, 342–370.

Gadsden, J.A. (1975) Infrared Spectra of Minerals and Related Inorganic Compounds, 277 p. Butterworths, London.

Guggenheim, S. and Eggleton, R.A. (1988) Crystal chemistry, classification, and identification of modulated layered silicates. In S.W. Bailey, Ed., Hydrous Phyllosilicates (exclusive of micas), 19, p. 675–725 . Reviews in Mineralogy, Mineralogical Society of America, Chantilly, Virginia.

Jakobsen, H., Nielsen, N., and Lindgreen, H. (1995) Sequences of charged sheets in rectorite. American Mineralogist, 80, 247–252.

Koski, R.A., Londsdale, P.F., Shanks, W.C., Berndt, M.E., and Howe, S. (1985) Mineralogy and geochemistry of a sediment-hosted hydrothermal sulfide deposit from the Southern trough of Guaymas basin, Gulf of California. Journal of Geophysical Research, 90, 6695–6707.

Koski, R.A., Benninger, L.M., Zierenberg, R.A., and Jonasson, I.R. (1994) Composition and growth history of hydrothermal deposits in Escanaba Trough, southern Gorda Ridge. In J.L. Morton, R.A. Zierenberg, and C.A. Reiss, Eds., Geologic, hydrothermal, and biological studies at escanaba Trough, Gorda Ridge, Offshore Northern California, p. 293–324. U.S. Geological Survey Bulletin, v. 2022.

Lackschewitz, K.S., Botz, R., Garbe-Schönberg, D., Scholten, J., and Stoffers, P. (2006) Mineralogy and geochemistry of clay samples from active hydrothermal vents off the north coast of Iceland. Marine Geology, 225, 177–190.

Léveillé, R.J., Longstaff, F.J., and Fyfe, W.S. (2002) Kerolite in carbonate-rich speleothems and microbial deposits from basaltic caves, Kauai, Hawaii. Clays and Clay Minerals, 50, 514–524.

Mackenzie, R.C. (1970) Simple phyllosilicates based on gibbsite- and brucite-like sheets. In R.C. Mackenzie, Ed., Differential Thermal Analysis, p. 497–537. Academic Press, London.

Martín de Vidales, J.L., Alia, J.M., García Navarro, F., and Rull, F. (1990) Caracteres estructurales de las fases interestratificadas irregularmente: Kerolita/Estevensita. Boletín de la Sociedad Española de Mineralogía, 13, 69–80.

Mehra, O.P. and Jackson, M.L. (1960) Iron oxide removal from soils and clays by dithionite-citrate system buffered with sodium bicarbonate. Clays and Clay Minerals, 7, 317–327.

Plançon, A. (2002) New modeling of X-ray diffraction by disordered lamellar structures, such as phyllosilicates. American Mineralogist, 87, 1672–1677.

Plançon, A. and Drits, V.A. (2000) Phase analysis of clays using an expert system and calculation programs for X-ray diffraction by two- and three-component mixed-layer minerals. Clays and Clays Minerals, 48, 57–62.

Pozo, M. and Casas, J. (1999) Origin of kerolite and associated Mg clays in palustrine-lacustrine environments. The Esquivias deposit (Neogene Madrid Basin, Spain). Clay Minerals, 34, 395–418.

Reynolds, Jr., R.C. and Reynolds, III, R.C. (1996) NEWMOD: The calculation of one-dimensional X-ray diffraction patterns of mixed-layer clay minerals. Computer program, Hanover, New Hampshire.

Russell, D.J. and Fraser, A.R. (1994) Infrared methods. In M.J. Wilson, Ed., Clay Mineralogy: Spectroscopic and Chemical Determinative Methods, p. 11–67. Chapman and Hall, London.

Von Damm, K.L., Parker, C.M., Zierenberg, R.A., Lilley, M.D., Olson, E.J., Clague, D.A., and McClain, J.S. (2005) The Escanaba Trough, Gorda Ridge hydrothermal system: Temporal stability and subseafloor complexity. Geochimica et Cosmochimica Acta, 69, 4971–4984.

Manuscript received May 10, 2007
Manuscript accepted February 18, 2008
Manuscript handled by Paul Schroeder